

Image-on-Scalar Regression via Deep Neural Networks

Daiwei Zhang

Dpt. of Biostatistics
University of Michigan
Ann Arbor, MI 48109
daiweiz@umich.edu

Lexin Li

Dpt. of Biostatistics
University of California
Berkeley, CA 94720
lexinli@berkeley.edu

Chandra Sripada

Dpt. of Psychairtry and Philosophy
University of Michigan
Ann Arbor, MI 48109
sripada@umich.edu

Jian Kang*

Dpt. of Biostatistics
University of Michigan
Ann Arbor, MI 48109
jiankang@umich.edu

Abstract

In medical imaging studies, a topic of central interest is the association analysis of massive imaging data with covariates of interest. The difficulty arises from the ultrahigh imaging dimensions, heterogeneous noises, and limited number of training images. To address these challenges, we propose a novel and conceptually straightforward neural network-based image-on-scalar regression model, in which the spatially varying functions of the main effects, individual deviations, and noise variances are all constructed through neural networks. Compared with existing methods, our method can identify a wider variety of spatial patterns, better captures the individual-wise heterogeneity, and is less affected by a small number of individuals. We provide estimation and selection algorithms with theoretically guaranteed asymptotic properties when the number of voxels grows faster than the number of individuals. We demonstrate the efficacy of our method through extensive simulation studies and the analysis of the fMRI data in the Autism Brain Imaging Data Exchange study and the Adolescent Brain Cognitive Development study.

Key words: brain imaging, fMRI, functional data analysis, high-dimensional inference, model selection, neural networks.

*To whom correspondence should be addressed

1 Introduction

1.1 Background

With the rapid growth of medical imaging studies, it has become a scientific task of great importance to discover the patterns of the influence of potential factors on massive imaging data. Primary types of images include T1-weighted magnetic resonance imaging (MRI) data, contrast maps from task-based functional MRI, and the local summary statistics of resting functional MRI data, such as fractional amplitude of low-frequency fluctuations and weighted degree of network connectedness. A typical imaging dataset contains multiple individuals, with observations from each individual at spatial points (called voxels) in a large set (called a template) of predetermined locations inside a common volume (often three-dimensional). The statistical challenge is to develop a model that delineates the association of voxels or regions of interest (ROI) with a set of covariates of interests, such as demographic information, clinical characteristics, and other non-imaging measurements. We refer to this type of models as image-on-scalar regression models, where the images are regarded as a functional response variable whose mean value depends on a set of scalar predictive variables.

Several major challenges are associated with the image-on-regression models for medical imaging data. First, the spatial correlation between voxels can be highly complex. Due to biological and technological reasons, imaging signals are often contained in contiguous, sharp-edged regions that are sparsely distributed throughout the whole spatial volume (Chan and Shen, 2005; Tabelow et al., 2008; Chumbley and Friston, 2009). For example, in neuroimaging studies, it has been found that the association with fear is substantially higher in the amygdala than in other brain regions (Whalen et al., 2001). Second, the signals across individuals can be heterogeneous and might depend on unobserved variables. For example, underlying medical conditions and the psychological state at the time of scanning can

affect the outputs of functional MRI. Third, the number of individuals is often be limited in imaging studies, while the noise level can be rather high due to machine artifacts and imperfect preprocessing, which together produce relatively low signal-to-noise ratios. This limitation makes it particularly difficult to apply traditional machine learning methods to image-on-scalar regression problems, since methods such as deep learning rely on a large sample size to train their highly flexible models. This might partially explain the relatively scant success of applying artificial neural networks to imaging studies, as compared to other fields such as computer vision and natural language processing.

1.2 Related work and our contributions

Traditionally, the straightforward method for fitting the image-on-scalar regression is the mass univariate analysis (MUA). This approach fits a general linear model (GLM) at each voxel and obtains voxel-wise test statistics to identify the brain regions that are significantly associated with the covariate of interest, after applying a multiple testing adjustment method such as the Bonferonni correction or false discovery rate control (Benjamini and Yekutieli, 2001). A major limitation of MUA is that the spatial correlation is not accounted for, which can result in low power for detecting significant ROIs and may potentially increase the false positive rate. One way to incorporate spatial correlation into MUA is smoothing the imaging data through a kernel convolution before fitting the GLM. An example of this more sophisticated type of MUA is statistical parametric mapping (SPM), which utilizes random field theory to make classical inferences (Friston, 2003). However, performing MUA on these pre-smoothed data can lead to low accuracy and low efficiency in estimating and testing the covariates' effects (Chumbley et al., 2009). Adaptive smoothing methods for preprocessing (Yue et al., 2010) and estimation (Polzehl and Spokoiny, 2000; Qiu, 2007), which are especially powerful for detecting delicate patterns such as jump discontinuities, may improve the performance by reducing noise and preserving features.

Instead of modeling each voxel independently, one can collectively consider all the voxels of the outcome variable (and the coefficients) as a tensor (i.e. a multi-dimensional array) and impose certain sparsity structures. For example, parsimonious tensor response regression (Li and Zhang, 2017), assumes the response tensor to be sparse after some linear transformation and aims to separate material and immaterial information. Another example is sparse tensor response regression (STORE) (Sun and Li, 2017), which embeds element-wise sparsity and low-rankness on the coefficient tensor and is designed to handle both symmetric and asymmetric responses. A major challenge for this family of models when applied to medical imaging data, which often contains a large number of voxels, is the difficulty in developing dimension reduction techniques that are both accurate and computationally efficient.

Beside treating the voxels as independent points or collectively as multi-dimensional arrays, we can also consider them as discrete observations of spatially varying functions. This framework transforms the image-on-scalar regression problem into a functional data analysis (FDA) problem, in which both the outcome variable and the regression coefficients are spatially varying functions. FDA-based methods have been extensively investigated in environmental health, epidemiology, and ecology (Cressie and Cassie, 1993; Diggle et al., 1998; Gelfand et al., 2003), although in these methods the spatially varying functions are assumed to be smooth or continuously differentiable up to certain degrees. Recently, the spatially varying coefficient model (SVCMM) was developed to systematically incorporate both spatial smoothness and jump discontinuities (Zhu et al., 2014). The inclusion of jump discontinuities makes SVCMM especially useful for neuroimaging applications. It can also identify regions significantly associated with the covariates of interest by using a step-wise estimating procedure and the asymptotic Wald test. Alternatively, Chen et al. (2016) utilize a novel penalty functions to detect the significant ROIs. In contrast, Li et al. (2020) and Yu et al. (2020) use bivariate splines over triangulation to approximate the coefficient function,

while Gu et al. (2014) use spline smoothing to produce simultaneous confidence corridors. From the Bayesian perspective, Shi and Kang (2015) model the spatially varying functions as thresholded multiscale Gaussian processes, and Bussas et al. (2017) handle them as Gaussian processes with isotropic priors.

In this work, we propose a novel and conceptually straightforward neural network-based image-on-scalar regression model (NN-ISR), in which the spatially varying functions of the main effects, individual deviations, and noise variances are all constructed through neural networks. Moreover, the neural networks are trained across voxels instead of across individuals. Compared with existing methods, NN-ISR can identify a wider variety of spatial patterns, better captures the individual-wise heterogeneity, and is less limited by a small number of individuals. We provide algorithms for training NN-ISR with theoretically guaranteed bounds of the estimation and selection errors as the number of voxels approaches infinity while the number of individuals is fixed. We demonstrate the efficacy of our method through extensive simulation studies and the analysis of the Autism Brain Imaging Data Exchange (ABIDE) data (Di Martino et al., 2014) and the Adolescent Brain Cognitive Development (ABCD) data (Casey et al., 2018).

The remainder of the manuscript is organized as follows. We introduce the NN-ISR model (Section 2.1), develop parameter estimation and feature selection algorithms (Section 2.2), and establish the theoretical properties (Section 2.3). Then NN-ISR will be evaluated against existing methods via simulation studies (Section 3.1) and analyses of the ABCD and ABIDE data (Section 3.2). We conclude with a brief discussion (Section 4).

2 Method

2.1 The functional image-on-scalar regression model

We first describe the data generation model by using the FDA framework. For individual $m \in 1, \dots, M$, let the response $y_m(\cdot)$ be a function with domain $\mathcal{D} \subset \mathbb{R}^K$ (the spatial volume) and range $\mathcal{E} \subset \mathbb{R}$, and let $\mathbf{x}_m \in \mathbb{R}^Q$ be the covariate vector. We assume that at each spatial location $\mathbf{d} \in \mathcal{D}$, the following relation holds:

$$y_m(\mathbf{d}) = \mathbf{x}_m^\top \boldsymbol{\beta}^*(\mathbf{d}) + \alpha_m^*(\mathbf{d}) + \epsilon_m(\mathbf{d}),$$

where $\boldsymbol{\beta}^*(\cdot) : \mathcal{D} \rightarrow \mathcal{E}^Q$ is the coefficient function of the main effects, and $\alpha_m^*(\cdot) : \mathcal{D} \rightarrow \mathcal{E}$ represents the individual response's deviation from $\mathbf{x}_m^\top \boldsymbol{\beta}^*(\cdot)$, and $\epsilon_m(\cdot) : \mathcal{D} \rightarrow \mathcal{E}$ is the noise.

We impose the following assumptions on the model's functional variables. For the main effects, after \mathcal{D} is partitioned into a finite number of connected components, $\boldsymbol{\beta}^*(\cdot)$ is continuous inside each component, and $\mu(\{\mathbf{d} : \boldsymbol{\beta}^*(\mathbf{d}) \neq \mathbf{0}\}) \ll \mu(\mathcal{D})$, where μ denotes the Lebesgue measure. Moreover, we call $\alpha_m^*(\cdot)$ the individual effect and assume it to be unknown but fixed (which makes the common nomenclature "random effect" less appropriate in our context). For the noises, we assume that $E[\epsilon_m(\mathbf{d})] = 0$, $\text{Var}[\epsilon_m(\mathbf{d})] = \sigma^{2*}(\mathbf{d})$, and $\epsilon_m(\mathbf{d})$ is independent from $\epsilon_{m'}(\mathbf{d}')$ whenever $m \neq m'$ or $\mathbf{d} \neq \mathbf{d}'$.

For conciseness, we represent the model in the matrix form

$$\mathbf{y}(\mathbf{d}) = \mathbf{X}\boldsymbol{\beta}^*(\mathbf{d}) + \boldsymbol{\alpha}^*(\mathbf{d}) + \boldsymbol{\epsilon}(\mathbf{d}), \quad \text{Var}[\boldsymbol{\epsilon}(\mathbf{d})] = \mathbf{I}\sigma^{2*}(\mathbf{d}), \quad (1)$$

where $\mathbf{y}(\mathbf{d}) = [\mathbf{y}_m(\mathbf{d})]_{m=1}^M$, $\boldsymbol{\alpha}^*(\mathbf{d}) = [\alpha_m^*(\mathbf{d})]_{m=1}^M$, $\boldsymbol{\epsilon}(\mathbf{d}) = [\epsilon_m(\mathbf{d})]_{m=1}^M$, $\mathbf{X}^\top = [\mathbf{x}_m]_{m=1}^M$, and \mathbf{I} is the $M \times M$ identity matrix.

Although $\mathbf{y}(\cdot)$ is a function that takes any spatial coordinate in the volume $\mathcal{D} \subset \mathbb{R}^K$ as input, the response variable is only observed at a finite number of such spatial locations;

that is, the value of $\mathbf{y}(\cdot)$ is only available in the template $\mathcal{D}_V \subset \mathcal{D}$ that contains $|\mathcal{D}_V| = V$ voxels. Thus the data is $(\{\mathbf{y}(\mathbf{d}_v)\}_{v=1}^V, \mathbf{X})$.

2.2 Neural network-based image-on-scalar regression

We begin with the definition of the feed-forward neural network (NN) and the related notations for the NN architecture.

Definition 1 (Neural network). A G -layer NN \aleph is a function with domain \mathbb{R}^{R_0} and range $\mathbb{R}^{R_{G+1}}$ that has the form

$$\aleph(\mathbf{d}|\mathbf{W}_0, \dots, \mathbf{W}_G, \mathbf{b}_0, \dots, \mathbf{b}_G) = \aleph(\mathbf{d}|\boldsymbol{\theta}) = \phi \left[\cdots \phi \left[\mathbf{d}^\top \mathbf{W}_0 + \mathbf{b}_0 \right]^\top \mathbf{W}_1 + \mathbf{b}_1 \cdots \right]^\top \mathbf{W}_G + \mathbf{b}_G,$$

where ϕ is a predetermined element-wise activation function (e.g. sigmoid, ReLU), $\mathbf{d} \in \mathbb{R}^{R_0}$ is the input variable, and for $j \in 1, \dots, G$, the weight and bias parameters of the j^{th} layer are $\mathbf{W}_j \in \mathbb{R}^{R_j \times R_{j+1}}$ and $\mathbf{b}_j \in \mathbb{R}^{1 \times R_j}$, respectively. For conciseness, the collection of all the parameters is denoted as $\boldsymbol{\theta} = (\mathbf{W}_0, \mathbf{b}_0, \dots, \mathbf{W}_G, \mathbf{b}_G)$, which is of dimension $\dim(\boldsymbol{\theta}) = \sum_{j=0}^G (R_j + 1) R_{j+1}$ and takes value in the parameter space $\Theta = \mathbb{R}^{\dim(\boldsymbol{\theta})}$. The architecture of the NN is denoted as $\text{arch}(\boldsymbol{\theta}) = (R_0, \dots, R_{G+1})$, and the number of nodes in the NN is denoted as $\#\text{nodes}(\boldsymbol{\theta}) = \sum_{j=1}^G R_j$.

Neural network approximation. In (1), our main interest is in estimating $\beta^*(\cdot)$, while $\alpha^*(\cdot)$ and $\sigma^{2*}(\cdot)$ are nuisance parameters. Instead of working with these infinite-dimensional parameters directly, we approximate $\beta^*(\cdot)$, $\alpha^*(\cdot)$ and $\sigma^2(\cdot)$ with three NNs that take the K -dimensional spatial coordinate as the input variable, namely $\aleph(\cdot|\boldsymbol{\theta})$, $\aleph(\cdot|\boldsymbol{\eta})$ and $\exp[\aleph(\cdot|\boldsymbol{\tau})]$, respectively, where $\text{arch}(\boldsymbol{\theta}) = \{K, R_1, R_2, \dots, R_G, Q\}$, $\text{arch}(\boldsymbol{\eta}) = \{K, S_1, S_2, \dots, S_H, M\}$, and $\text{arch}(\boldsymbol{\tau}) = \{K, T_1, T_2, \dots, T_J, 1\}$. This approximation leads to the NN-ISR model

$$\mathbf{y}(\mathbf{d}) = \mathbf{X}\aleph(\mathbf{d}|\boldsymbol{\theta}) + \aleph(\mathbf{d}|\boldsymbol{\eta}) + \boldsymbol{\epsilon}(\mathbf{d}), \quad \text{Var}[\boldsymbol{\epsilon}(\mathbf{d})] = \mathbf{I} \exp[\aleph(\mathbf{d}|\boldsymbol{\tau})], \quad (2)$$

where the NN parameters $\boldsymbol{\theta}, \boldsymbol{\eta}, \boldsymbol{\tau}$ are to be estimated from the data $(\{\mathbf{y}(\mathbf{d}_v)\}_{v=1}^V, \mathbf{X})$. To this end, we minimize the following penalized weighted L_2 loss function:

$$(\hat{\boldsymbol{\theta}}, \hat{\boldsymbol{\eta}}, \hat{\boldsymbol{\tau}}) = \underset{(\boldsymbol{\theta}, \boldsymbol{\eta}, \boldsymbol{\tau}) \in \boldsymbol{\Theta}}{\operatorname{argmin}} \left\{ \sum_{v=1}^V \frac{\|\mathbf{y}(\mathbf{d}_v) - \mathbf{X}\aleph(\mathbf{d}_v|\boldsymbol{\theta}) - \aleph(\mathbf{d}_v|\boldsymbol{\eta})\|_2^2}{\exp[-\aleph(\mathbf{d}_v|\boldsymbol{\tau})]} + L(\boldsymbol{\theta}, \boldsymbol{\eta}, \boldsymbol{\tau}) \right\}, \quad (3)$$

where $\boldsymbol{\Theta} = \mathbb{R}^{\dim(\boldsymbol{\theta})} \times \mathbb{R}^{\dim(\boldsymbol{\eta})} \times \mathbb{R}^{\dim(\boldsymbol{\tau})}$ and $L(\boldsymbol{\theta}, \boldsymbol{\eta}, \boldsymbol{\tau}) = \lambda_\theta \|\boldsymbol{\theta}\|_2^2 + \lambda_\eta \|\boldsymbol{\eta}\|_2^2 + \lambda_\tau \|\boldsymbol{\tau}\|_2^2$ for some pre-specified tuning parameters λ_θ , λ_η and λ_τ . The NN parameter estimate $\hat{\boldsymbol{\theta}}$ leads to an estimate of the spatially varying coefficient function for the main effects $\hat{\boldsymbol{\beta}}(\cdot) = \aleph(\cdot|\hat{\boldsymbol{\theta}})$.

Neural network tuning. For choosing the weights of the penalty terms, we suggest setting $\lambda_\eta, \lambda_\tau \geq 10\lambda_\theta$ (to avoid overfitting or unstable optimization), conducting cross validation with a sequence of exponentially increasing λ_θ , and selecting the optimal value that produces the least image recovery error $\|\mathbf{y}_{\text{validation}} - \mathbf{X}_{\text{validation}}\aleph(\mathbf{d}|\hat{\boldsymbol{\theta}})\|_2^2$ on the validation data. For choosing the NN architecture, we suggest starting with excessive width and depth, and then keep halving the width and depth simultaneously until the validation loss increases significantly. In our experiments, we found that using 16 layers with 256 nodes in each layer is more than needed in every experimental setting. As we gradually reduced the complexity of the NN, the performance was not noticeably affected until the depth was reduced to 3 and the width to 32.

Estimation algorithm. To find the optimal NN parameters in (2), we employ NN-ISR model fitting procedure in Algorithm 1. To initialize the algorithm, we set the individual effects $\hat{\boldsymbol{\alpha}}(\cdot)$ with zeros and the noise variance $\hat{\sigma}^2(\cdot)$ with ones. The first step in each iteration is computing the MUA estimate $\tilde{\boldsymbol{\beta}}(\mathcal{D}_V)$ with $\boldsymbol{\alpha}(\hat{\mathcal{D}}_V)$ subtracted from the response images $\mathbf{y}(\mathcal{D}_V)$. Then the main effect NN $\aleph(\cdot|\hat{\boldsymbol{\theta}})$ is trained to fit $\tilde{\boldsymbol{\beta}}(\mathcal{D}_V)$ by using stochastic gradient descent (SGD) (Bottou, 2010). In our context, each SGD minibatch \mathcal{D}_U is a set of U voxels (as opposed to a set of individuals), randomly selected from all the V voxels in the template \mathcal{D}_V .

The weight of each voxel sample is inversely proportional to its estimated noise variance. The SGD learning is done independently L times, where each time the SGD chain starts from a different randomly selected initial value. At the end, the optimal NNs from the L SGD chains are averaged to obtain a more stable estimate of the main effects $\hat{\beta}(\cdot) = L^{-1} \sum_{l=1}^L \aleph(\cdot | \hat{\theta}^{(l)})$. Next, the individual effect NN $\alpha(\cdot | \hat{\eta})$ is trained to fit $\mathbf{y}(\mathcal{D}_V) - \mathbf{X}\hat{\beta}(\mathcal{D}_V)$ by using SGD, with the sample weight inversely proportional to the estimated noise variance. Finally, the variance noise NN $\aleph(\cdot | \hat{\eta})$ is updated by SGD to learn the variances of the residuals $\mathbf{y}(\mathcal{D}_V) - \mathbf{X}\hat{\beta}(\mathcal{D}_V) - \hat{\alpha}(\mathcal{D}_V)$. This procedure is repeated until $\hat{\beta}(\mathcal{D}_V)$ changes no more than a predetermined threshold or the maximal number of iterations is reached.

Selection algorithm. After the NN-ISR estimate of the main effects is obtained, we use Algorithm 2 to select the voxels with non-zero effects for each covariate. First, with the estimated individual effects $\hat{\alpha}(\mathcal{D}_V)$ subtracted from the response image $\mathbf{y}(\mathcal{D}_V)$, we find the MUA main effect estimate $\tilde{\beta}(\mathcal{D}_V)$ and compute its standard error $\text{SE}[\tilde{\beta}(\mathcal{D}_V)]$ by using the estimated noise variances $\hat{\sigma}^2(\mathcal{D})$. Then we conduct classical statistical testing for each voxel with the false-positive rate controlled at a . This gives us c_q , the proportion of voxels selected by MUA for covariate q , which we use as a conservative quantile cutoff for the NN-ISR estimate. That is, we select a voxel \mathbf{d}_v for covariate q if and only if its signal strength $|\hat{\beta}_q(\mathbf{d}_v)|$ among all the voxels of the NN-ISR main effect estimate $\{|\hat{\beta}_q(\mathbf{d}_1)|, \dots, |\hat{\beta}_q(\mathbf{d}_V)|\}$ has a quantile of c_q or higher.

2.3 Theoretical Properties

We now provide a theoretical analysis of the NN-ISR model. First, Theorem 1 shows that the mean squared error (MSE) of NN-ISR's main effect estimator in Algorithm 1 converges no more slowly than the estimation error of the general NN regression model with the same architecture. Based on this result, Theorem 2 proves that the same convergence rate holds for the mean signed error (MSiE) of the NN-ISR estimator in Algorithm 2. In Theorem 3, as

a special case, we provide an error bound for the one-layer NN regression model in general, which immediately gives us Corollary 4's bound of the one-layer NN-ISR's estimation MSE and MiSE. The proofs can be found in the Appendix.

The convergence rate of NN-ISR depends on the architecture of the NNs used in the model and how the estimation error of NNs with such architecture converges in the general NN regression problem, as described in the following definition:

Definition 2 (Estimation error bound for general neural network regression). Suppose $\{(\mathbf{x}_n, \mathbf{y}_n)\}_{n=1}^N$ are independent samples generated from the model $\mathbf{y}_n = \mathbf{f}^*(\mathbf{x}_n) + \boldsymbol{\epsilon}_n$ with $\mathbb{E}[\boldsymbol{\epsilon}_n] = \mathbf{0}$, where $f^* : \mathbb{R}^K \rightarrow \mathbb{R}^Q$ is the function of interest. By using the notations in Definition 1, the general arch($\boldsymbol{\theta}$)-neural network regression model is $\mathbf{y}_n = \aleph(\mathbf{x}_n|\boldsymbol{\theta}) + \boldsymbol{\epsilon}_n$, where $\aleph(\cdot|\boldsymbol{\theta})$ is any NN with architecture arch($\boldsymbol{\theta}$). The optimal NN parameter is

$$\hat{\boldsymbol{\theta}} = \underset{\boldsymbol{\theta} \in \mathbb{R}^{\dim(\boldsymbol{\theta})}}{\operatorname{argmin}} \left\{ \sum_{n=1}^N \|\mathbf{y}(\mathbf{x}_n) - \aleph(\mathbf{x}_n|\boldsymbol{\theta})\|_2^2 + L(\boldsymbol{\theta}) \right\},$$

where $L(\cdot)$ is a regularization function that satisfies $\int_{\boldsymbol{\theta} \in \mathbb{R}^{\dim(\boldsymbol{\theta})}} \exp\{-L(\boldsymbol{\theta})\} d\boldsymbol{\theta} < \infty$. Then an upper bound of the estimation error for the general arch($\boldsymbol{\theta}$)-neural network regression model is a function $\psi_{\text{arch}(\boldsymbol{\theta})}(\cdot)$ that satisfies

$$\mathbb{E} \left\{ \frac{1}{N} \sum_{n=1}^N \left\| \aleph(\mathbf{x}_n|\hat{\boldsymbol{\theta}}) - \mathbf{f}^*(\mathbf{x}_n) \right\|_2^2 \right\} = \mathcal{O} [\psi_{\text{arch}(\boldsymbol{\theta})}(N)].$$

Now, we show that the main effect estimator obtained from the procedure in Algorithm 1 converges no more slowly than the estimator in the general NN regression model with the same NN architecture. Moreover, the estimation MSE decreases as the *product* of the numbers of voxels and individuals increases. A notable result of Theorem 1 is that the estimation error can be reduced by increasing the number of voxels without increasing the number of individuals. In practice, the implication is that in a medical imaging study where the number of individuals is limited, the NN-ISR model can still be made arbitrarily accurate if the

resolution of the imaging can be made arbitrarily high.

Theorem 1. *Suppose an M -individual, V -voxel data set generated by the model in (1) is used to train the NN-ISR model in (2), where the main effect neural network $\aleph(\cdot|\boldsymbol{\theta})$ has architecture $\text{arch}(\boldsymbol{\theta})$. Assume the estimation error for the general $\text{arch}(\boldsymbol{\theta})$ -neural network regression model with a sample size of N is bounded above by $\psi_{\text{arch}(\boldsymbol{\theta})}(N)$ (as defined in Definition 2). Then the estimator $\hat{\boldsymbol{\beta}}(\cdot)$ in Algorithm 1 has error bound*

$$\mathbb{E} \left\{ \frac{1}{V} \sum_{v=1}^V \left\| \hat{\boldsymbol{\beta}}(\mathbf{d}_v) - \boldsymbol{\beta}^*(\mathbf{d}_v) \right\|_2^2 \right\} = \mathcal{O} [\psi_{\text{arch}(\boldsymbol{\theta})}(MV)] .$$

Moreover, Theorem 2 shows that the same error bound holds for the MSiE of the selection estimator in Algorithm 2, so the probability of correctly identifying the main effect sign of an arbitrarily high proportion of the voxels approaches one as the product of the numbers of individuals and voxels approaches infinity. Thus for any ROI, the probability of successfully detecting its significance and the direction of its effect can be made arbitrarily high even if the number of individuals is limited, provided that the imaging resolution keeps increasing.

Theorem 2. *Suppose the same conditions as in Theorem 1. Then for any $\delta > 0$ there exists a selection relaxedness $a \in [0, 1]$ such that the estimator $\bar{\boldsymbol{\beta}}(\cdot)$ in Algorithm 2 satisfies*

$$\Pr \left[\frac{1}{V} \sum_{v=1}^V \left\| \text{sign}[\bar{\boldsymbol{\beta}}(\mathbf{d}_v)] - \text{sign}[\boldsymbol{\beta}^*(\mathbf{d}_v)] \right\|_0 \geq \delta \right] = \mathcal{O} [\psi_{\text{arch}(\boldsymbol{\theta})}(MV)] .$$

Theorems 1 and 2 show that the convergence of the MSE and MSiE of the NN-ISR main effect estimator is a function of the product of the numbers of individuals and voxels. This result can be applied to neural networks of any architecture with a proven estimation error bound. As an example, Theorem 3 establishes such an error bound for fitting a one-layer NN regression model in general.

Theorem 3. *Suppose $\text{arch}(\boldsymbol{\theta})$ is a one-layer, R -node neural network architecture . The*

estimation error for the general $\text{arch}(\boldsymbol{\theta})$ -neural network regression model (as defined in Definition 2) with a sample size of N is bounded above by

$$\psi_{\text{arch}(\boldsymbol{\theta})}(N) = \mathcal{O} \left[\frac{1}{R} + \frac{R \log N}{N} \right].$$

It has been shown that the error bound in Theorem 3 holds for the one-layer NN regression model with a *random design* (Barron, 1991, 1994; McCaffrey and Gallant, 1994), where the input samples are random and the estimation error is integrated over the input sample space. We establish the same error bound for the one-layer NN regression model with a *fixed design*, as described in Definition 2. Our estimation error is equivalent to a Riemann sum of the estimation error in Barron (1991).

An immediate consequence of Theorem 3 is an error bound for the one-layer NN-ISR model, which converges almost linearly toward zero with respect to the product of the numbers of individuals and voxels, as shown in Corollary 4.

Corollary 4. *Suppose the same conditions as in Theorems 1 and 2. If the NN-ISR model's main effect neural network has a one-layer, R -node architecture, then*

$$\begin{aligned} \mathbb{E} \left\{ \frac{1}{V} \sum_{v=1}^V \left\| \hat{\boldsymbol{\beta}}(\mathbf{d}_v) - \boldsymbol{\beta}^*(\mathbf{d}_v) \right\|_2^2 \right\} &= \mathcal{O} \left[\frac{1}{R} + \frac{R \log MV}{MV} \right] \\ \Pr \left[\frac{1}{V} \sum_{v=1}^V \left\| \text{sign}[\bar{\boldsymbol{\beta}}(\mathbf{d}_v)] - \text{sign}[\boldsymbol{\beta}^*(\mathbf{d}_v)] \right\|_0 \geq \delta \right] &= \mathcal{O} \left[\frac{1}{R} + \frac{R \log MV}{MV} \right]. \end{aligned}$$

3 Experiments

3.1 Simulation studies

Setup. Images of resolution $64 \times 64 \times 8$ were generated by 3 covariates according to (1). The covariates were independently sampled from $\mathcal{N}(0, 1)$. The experiments were conducted by varying the main effect pattern, noise distribution, and number of individuals. For the

main effects, we used either the piecewise continuous (PT) design or the piecewise constant (PT) design (Zhu et al., 2014), as illustrated in Figure 1. The noises were drawn from either $\mathcal{N}(0, 1)$ or $\chi_3^2 - 3$, and the number of individuals was set to 50 or 100. In addition, each individual effect followed a radial pattern design. (See the Appendix for more a more detailed description of data design). Each experimental setting was replicated 50 times.

We compared the performance of NN-ISR with MUA and SVCM. Estimation accuracy was evaluated by the median and inter-quadrantic range (IQR) of the main effect estimation MSE. Selection accuracy was measured by the average receiver operating characteristic curve (ROC) and its area under curve (AUC). For NN-ISR, we used an NN of depth 4 and width 128 for each main effect and an NN of depth 1 and width 16 for each individual effect. The regularization parameters for the main and individual effects were 10^{-3} and 10^{-2} , respectively.

Results. NN-ISR produced the least noisy estimate compared with MUA and SVCM, as seen in Figure 1. Quantitatively, NN-ISR achieved the lowest MSEs and the narrowest IQRs for estimating the main effects in all experimental settings (Table 1). For selection accuracy, NN-ISR had the highest AUCs in all cases, where a selection of the ROC plots are shown in Figure 2. The advantage of NN-ISR was more distinct on the more noisy and skewed data.

3.2 Analysis of fMRI data

Setup. Our work was motivated by the needs of analyzing the fMRI data from two large neuroimaging consortia: ABIDE (Di Martino et al., 2014) and ABCD (Casey et al., 2018). Both studies collected fMRI images and assessed cognitive ability (CA) and other clinical characteristics from multiple U. S. experimental sites. Our analysis focused on the association between brain activity and CA. We divided the brain volume into parcels based on the automated anatomical labeling (AAL) atlas (Tzourio-Mazoyer et al., 2002) and grouped the parcels into functional networks. Then NN-ISR was used to select the functional networks

most significantly associated with CA.

To evaluate the performance of NN-ISR against the other methods, we conducted site-wise cross validation. For each fold of the cross validation, one experimental site was selected to provide the samples for training the models. Each method was then evaluated by the squared correlation between its predicted images and the true images (without the individual effects) on the rest of the sites. We also applied each method to select the most significant voxels and compared the number and average size of contiguous clusters of selected voxels, since larger ROIs are more interpretable and reproducible in neuroimaging studies.

For NN-ISR tuning, we used an architecture of 6 layers with 128 nodes in each layer. We verified the model’s insensitivity to the choice of architecture after observing the lack of noticeable change in the predicted testing images when the depth and/or width of the NN were doubled or halvened. For selecting the penalty terms, we first applied ridge regression (Marquardt and Snee, 1975) with 5-fold cross-validation on the training set and used its optimal L_2 penalty weight as the initial value for NN-ISR’s main effect penalty weight. The individual effect and noise variance penalty weights were fixed to 10 times of that of the main effects. We then fit NN-ISR multiple times with the weights varying from 1/1000 to 100 times of their initial values and selected the one with the best cross validation performance on the training set.

ABIDE aimed at improving the neurological understanding of autism and the associated cognitive behaviors. In Phase I of the study, 20 resting-state fMRI datasets from 17 experimental sites were aggregated, resulting in a total of 1,112 subjects. In our analysis, we employed a widely adopted fMRI processing pipeline (Craddock et al., 2013; He et al., 2019). For the response image, we used the weighted degrees of network connectedness, which correspond to each voxel’s number of direct connections to the other voxels. Among the covariates, we were most interested in the effect of the CA, as measured by the full-scale

intelligence quotient. Age, sex, and autism diagnostic score were adjusted for. After the missing values were removed, the dataset contained 821 subjects.

ABCD focused on studying the association between cognitive behaviors and brain development. This study collected the brain images and various CA assessment scores of more than 11,800 children of age 9 to 10 from 21 experimental sites. Our analysis used the minimally preprocessed 0-back task-based fMRI data of 1991 subjects from the curated ABCD annual release 1.1 (Hagler Jr et al., 2019). The response image was the 0-back task contrast map. In this task, brain activation that engages memory regulation processes and cognitive functions were found reliably across subjects. The covariate of interest, CA, was measured by the general CA component score (Sripada et al., 2019). Age, sex, and psychiatric diagnostic score were adjusted for.

Cognitive ability-associated functional regions. NN-ISR selected similar functional brain regions in ABIDE and ABCD, with the following having the highest proportion of voxels selected in both datasets: visual (Calcarine_L, Cuneus_R, Lingual_L&R) default mode (Occipital_Mid_R, Temporal_Mid_R, Frontal_Med_Orb_L&R), dorsal attention (Temporal_Mid_R, Parietal_Sup_L, Postcentral_L), and ventral attention (Temporal_Mid_L, Temporal_Sup_L&R), as shown in Figure 3. This result is consistent with findings in the existing literature, which has identified the visual (Hearne et al., 2016) and attention networks (Wu et al., 2013; Hilger et al., 2017; Van Den Heuvel et al., 2009) to be associated with intelligence. In comparison, although MUA and SVCN identified similar brain regions in ABCD, they were unable to detect signals for the default mode and dorsal attention regions in ABIDE.

Image recovery and selection contiguousness comparisons. Among the methods studied, NN-ISR achieved the highest medians and narrowest IQRs for image recovery correlation squared in the site-wise cross validation, as reported in Figures 4a and 4b. The advantage of NN-ISR was more distinct in ABIDE than that in ABCD. Figures 4c and 4d

show the number of contiguous selection clusters versus the log mean cluster sizes. NN-ISR selected fewer regions with larger sizes compared to MUA and SVCMM. These results indicate that NN-ISR extracted more useful spatial location information for model inferences than the other methods.

4 Discussion

In this work, we have presented the novel method NN-ISR that utilizes neural networks to perform estimation and selection for the spatially varying coefficient function of the main effects in image-on-scalar regression. This neural network-based estimator is flexible enough to approximate a wide range of sparse and piecewise-continuous spatially varying functions. We have developed model fitting algorithms for NN-ISR with theoretically guaranteed estimation and selection error bounds, which can be reduced arbitrarily small without increasing the number of individuals, provided the imaging resolution is sufficiently high. In the special case of one-layer neural networks, the errors shrink almost linearly toward zero as the number of voxels approaches infinity. We have demonstrated that NN-ISR outperforms the existing alternatives on extensive simulation studies and on the fMRI data of two large neuroimaging consortium studies. In addition, our model and algorithm are conceptually straightforward and can be easily implemented and modified on common deep learning software platforms.

References

- Barron, A. R. (1991). Complexity regularization with application to artificial neural networks. In *Nonparametric functional estimation and related topics*, pages 561–576. Springer.
- Barron, A. R. (1994). Approximation and estimation bounds for artificial neural networks. *Machine Learning* **14**, 115–133.
- Benjamini, Y. and Yekutieli, D. (2001). The control of the false discovery rate in multiple testing under dependency. *Annals of Statistics* pages 1165–1188.
- Bottou, L. (2010). Large-scale machine learning with stochastic gradient descent. In *Proceedings of COMPSTAT’2010*, pages 177–186. Springer.
- Bussas, M., Sawade, C., Kühn, N., Scheffer, T., and Landwehr, N. (2017). Varying-coefficient models for geospatial transfer learning. *Machine Learning* **106**, 1419–1440.
- Casey, B., Cannonier, T., Conley, M. I., Cohen, A. O., Barch, D. M., Heitzeg, M. M., Soules, M. E., Teslovich, T., Dellarco, D. V., Garavan, H., et al. (2018). The adolescent brain cognitive development (abcd) study: imaging acquisition across 21 sites. *Developmental Cognitive Neuroscience* **32**, 43–54.
- Chan, T. F. and Shen, J. (2005). *Image processing and analysis: variational, PDE, wavelet, and stochastic methods*. SIAM.
- Chen, Y., Wang, X., Kong, L., and Zhu, H. (2016). Local region sparse learning for image-on-scalar regression. *arXiv preprint arXiv:1605.08501*.
- Chumbley, J., Worsley, K. J., Flandin, G., and Friston, K. J. (2009). False discovery rate revisited: Fdr and topological inference using gaussian random fields. *NeuroImage* **44**, 62–70.

- Chumbley, J. R. and Friston, K. J. (2009). False discovery rate revisited: Fdr and topological inference using gaussian random fields. *Neuroimage* **44**, 62–70.
- Craddock, C., Sikka, S., Cheung, B., Khanuja, R., Ghosh, S. S., Yan, C., Li, Q., Lurie, D., Vogelstein, J., Burns, R., Colcombe, S., Mennes, M., Kelly, C., Di Martino, A., Castellanos, F. X., and Milham, M. (2013). Towards automated analysis of connectomes: The configurable pipeline for the analysis of connectomes (c-pac). *Frontiers in Neuroinformatics*.
- Cressie, N. A. and Cassie, N. A. (1993). *Statistics for Spatial Data*, volume 900. Wiley New York.
- Di Martino, A., Yan, C.-G., Li, Q., Denio, E., Castellanos, F. X., Alaerts, K., Anderson, J. S., Assaf, M., Bookheimer, S. Y., Dapretto, M., et al. (2014). The autism brain imaging data exchange: towards a large-scale evaluation of the intrinsic brain architecture in autism. *Molecular Psychiatry* **19**, 659–667.
- Diggle, P. J., Tawn, J., and Moyeed, R. (1998). Model-based geostatistics. *Journal of the Royal Statistical Society: Series C (Applied Statistics)* **47**, 299–350.
- Friston, K. J. (2003). Statistical parametric mapping. In *Neuroscience databases*, pages 237–250. Springer.
- Gelfand, A. E., Kim, H.-J., Sirmans, C., and Banerjee, S. (2003). Spatial modeling with spatially varying coefficient processes. *Journal of the American Statistical Association* **98**, 387–396.
- Gu, L., Wang, L., Härdle, W. K., and Yang, L. (2014). A simultaneous confidence corridor for varying coefficient regression with sparse functional data. *TEST* **23**, 806–843.

- Hagler Jr, D. J., Hatton, S., Cornejo, M. D., Makowski, C., Fair, D. A., Dick, A. S., Sutherland, M. T., Casey, B., Barch, D. M., Harms, M. P., et al. (2019). Image processing and analysis methods for the adolescent brain cognitive development study. *NeuroImage* **202**, 116091.
- He, K., Xu, H., and Kang, J. (2019). A selective overview of feature screening methods with applications to neuroimaging data. *Wiley Interdisciplinary Reviews: Computational Statistics* **11**, e1454.
- Hearne, L. J., Mattingley, J. B., and Cocchi, L. (2016). Functional brain networks related to individual differences in human intelligence at rest. *Scientific Reports* **6**, 32328.
- Hilger, K., Ekman, M., Fiebach, C. J., and Basten, U. (2017). Efficient hubs in the intelligent brain: Nodal efficiency of hub regions in the salience network is associated with general intelligence. *Intelligence* **60**, 10–25.
- Kingma, D. P. and Ba, J. (2014). Adam: A method for stochastic optimization. *arXiv preprint arXiv:1412.6980*.
- Li, L. and Zhang, X. (2017). Parsimonious tensor response regression. *Journal of the American Statistical Association* **112**, 1131–1146.
- Li, X., Wang, L., Wang, H. J., and Initiative, A. D. N. (2020). Sparse learning and structure identification for ultrahigh-dimensional image-on-scalar regression. *Journal of the American Statistical Association* pages 1–15.
- Marquardt, D. W. and Snee, R. D. (1975). Ridge regression in practice. *The American Statistician* **29**, 3–20.
- McCaffrey, D. F. and Gallant, A. R. (1994). Convergence rates for single hidden layer feedforward networks. *Neural Networks* **7**, 147–158.

- Polzehl, J. and Spokoiny, V. G. (2000). Adaptive weights smoothing with applications to image restoration. *Journal of the Royal Statistical Society: Series B (Statistical Methodology)* **62**, 335–354.
- Qiu, P. (2007). Jump surface estimation, edge detection, and image restoration. *Journal of the American Statistical Association* **102**, 745–756.
- Shi, R. and Kang, J. (2015). Thresholded multiscale gaussian processes with application to bayesian feature selection for massive neuroimaging data. *arXiv preprint arXiv:1504.06074*.
- Sripada, C., Rutherford, S., Angstadt, M., Thompson, W. K., Luciana, M., Weigard, A., Hyde, L. H., and Heitzeg, M. (2019). Prediction of neurocognition in youth from resting state fmri. *Molecular Psychiatry* pages 1–9.
- Sun, W. W. and Li, L. (2017). Store: sparse tensor response regression and neuroimaging analysis. *The Journal of Machine Learning Research* **18**, 4908–4944.
- Tabelow, K., Polzehl, J., Spokoiny, V., and Voss, H. U. (2008). Diffusion tensor imaging: structural adaptive smoothing. *NeuroImage* **39**, 1763–1773.
- Tzourio-Mazoyer, N., Landeau, B., Papathanassiou, D., Crivello, F., Etard, O., Delcroix, N., Mazoyer, B., and Joliot, M. (2002). Automated anatomical labeling of activations in spm using a macroscopic anatomical parcellation of the mni mri single-subject brain. *Neuroimage* **15**, 273–289.
- Van Den Heuvel, M. P., Stam, C. J., Kahn, R. S., and Pol, H. E. H. (2009). Efficiency of functional brain networks and intellectual performance. *Journal of Neuroscience* **29**, 7619–7624.

- Whalen, P. J., Shin, L. M., McInerney, S. C., Fischer, H., Wright, C. I., and Rauch, S. L. (2001). A functional mri study of human amygdala responses to facial expressions of fear versus anger. *Emotion* **1**, 70.
- Wu, K., Taki, Y., Sato, K., Hashizume, H., Sassa, Y., Takeuchi, H., Thyreau, B., He, Y., Evans, A. C., Li, X., et al. (2013). Topological organization of functional brain networks in healthy children: differences in relation to age, sex, and intelligence. *PloS One* **8**,.
- Yu, S., Wang, G., Wang, L., and Yang, L. (2020). Multivariate spline estimation and inference for image-on-scalar regression. *Statistica Sinica* .
- Yue, Y., Loh, J. M., and Lindquist, M. A. (2010). Adaptive spatial smoothing of fmri images. *Statistics and its Interface* **3**, 3–13.
- Zhu, H., Fan, J., and Kong, L. (2014). Spatially varying coefficient model for neuroimaging data with jump discontinuities. *Journal of the American Statistical Association* **109**, 1084–1098.

Table 1: Median and inter-quartile range (IQR, in parentheses) of the mean squared error of the estimates by MUA, SVCM, and NN-ISR for the main effects in the simulation studies. The main effects follow either the piecewise continuous (PT) design or the piecewise constant (PS) design. For PT, evaluation conducted on each of the four zones, where each zone contains neither, one, or both of smooth-edged and sharp-edged activation regions. The number of individuals is set to $M = 50$ or $M = 100$. (Unit: 10^{-2} for PT, 10^{-3} for PS)

	$\mathcal{N}(0, 1)$ noise						$\chi_3^2 - 3$ noise					
	M = 50			M = 100			M = 50			M = 100		
	MUA	SVCM	NN-ISR	MUA	SVCM	NN-ISR	MUA	SVCM	NN-ISR	MUA	SVCM	NN-ISR
PT Null	53 (10)	24 (7)	9 (5)	25 (4)	10 (4)	4 (3)	50 (10)	23 (7)	8 (4)	26 (5)	11 (5)	4 (3)
PT Smooth	54 (10)	26 (8)	11 (7)	26 (5)	11 (4)	5 (3)	50 (10)	24 (8)	10 (6)	26 (4)	12 (3)	5 (2)
PT Sharp	52 (8)	25 (9)	11 (6)	25 (5)	11 (4)	7 (4)	49 (11)	23 (9)	11 (4)	26 (4)	12 (3)	7 (3)
PT Mixed	53 (8)	25 (10)	11 (6)	25 (4)	11 (4)	6 (3)	52 (12)	25 (10)	11 (7)	26 (5)	12 (3)	6 (3)
PS Overall	21 (1)	10 (1)	4 (1)	10 (1)	4 (0)	3 (1)	123 (3)	60 (13)	10 (3)	61 (0)	24 (5)	8 (4)

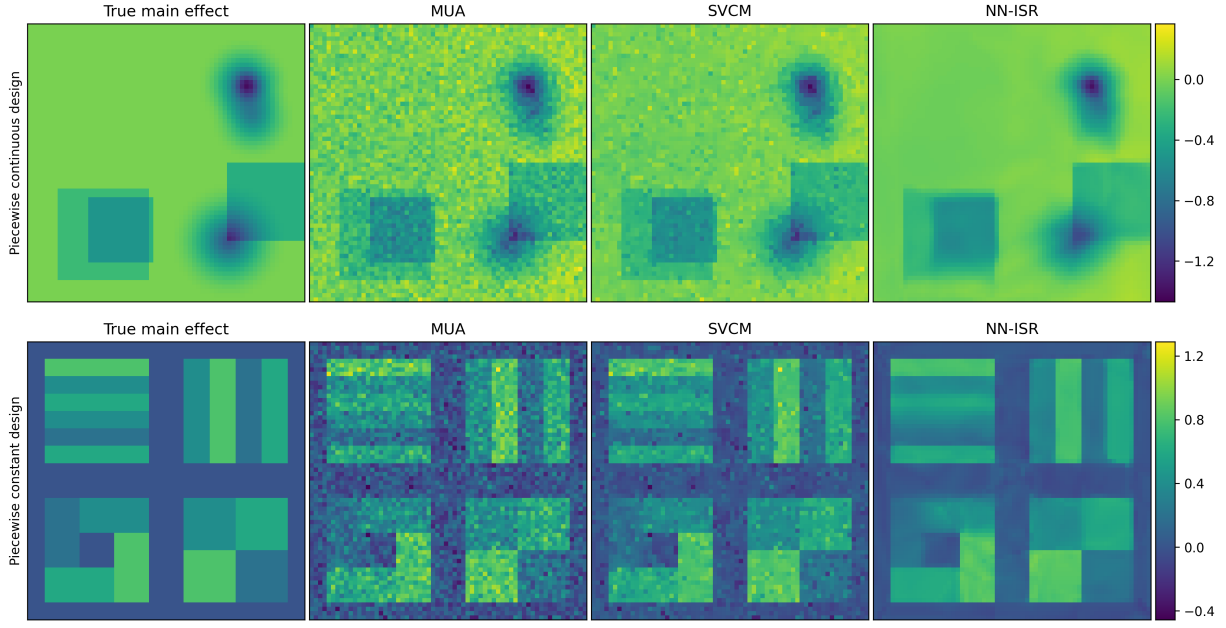


Figure 1: Slices of the true main effect (Col. 1) and the estimates by MUA (Col. 2), SVC (Col. 3), and NN-ISR (Col. 4) in the piecewise continuous (Row 1) and piecewise constant (Row 2) designs in the simulation studies.

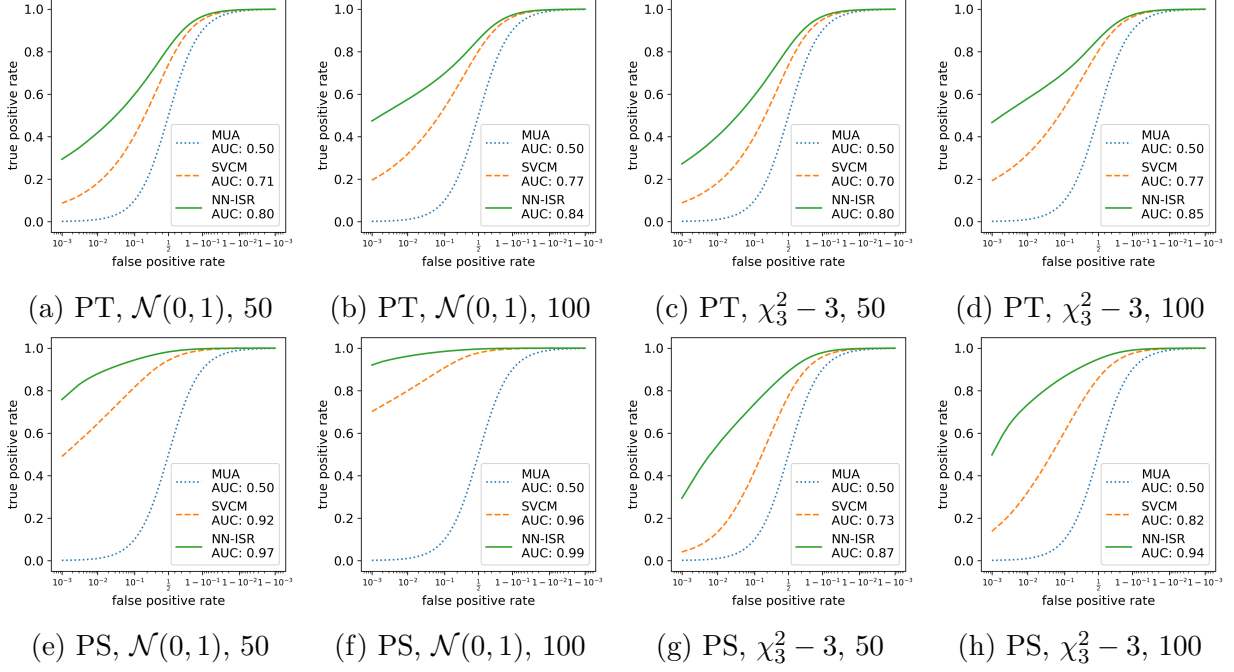


Figure 2: Average ROC and AUC in the simulation studies for each experimental setting. The main effect follow either the piecewise continuous (PT) design (a,b,c,d) or the piecewise constant (PS) design (e,f,g,h). Noises are drawn from $\mathcal{N}(0, 1)$ (a,b,e,f) or $\chi_3^2 - 3$ (c,d,g,h). The number of individuals is 50 (a,c,e,g) or 100 (b,d,f,h). Subcaptions indicate design, noise distribution, and sample size, respectively.

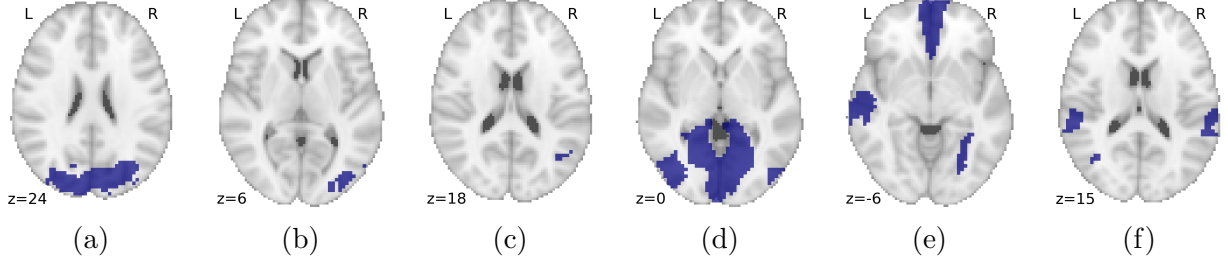


Figure 3: Voxels selected by NN-ISR for cognitive ability (CA) in the ABIDE (a,b,c) and ABCD (d,e,f) data inside the visual (a, d), default mode (b, e), dorsal (c) and ventral (f) attention networks. These four functional networks have the highest proportion of voxels selected in both datasets.

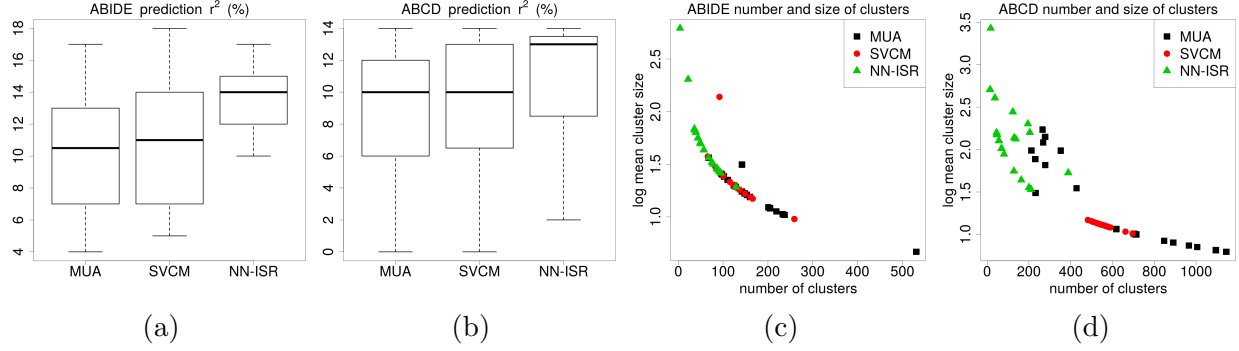


Figure 4: Estimation and selection evaluation for MUA, SVC, and NN-ISR in the analysis of ABIDE (a, c) and ABCD (b, d) data in cross-site testing. Each time one experimental site is chosen to provide the training samples and the other sites are used for testing. Estimation accuracy is measured by the image recovery prediction correlation squared (a, b). Selection contiguousness is evaluated by the number and average size of contiguous clusters of selected voxels for the main effect of cognitive ability (c, d), Larger activation regions with stronger signals are considered more interpretable and reproducible in neuroimaging studies.

Appendix A Algorithms

Algorithm 1: NN-ISR model estimation procedure

Input: data $\mathbf{X}, \mathbf{y}(\mathcal{D}_V) = \{\mathbf{y}(\mathbf{d}_v)\}_{v=1}^V$; neural network (NN) regularization weights $\lambda_\theta, \lambda_\eta, \lambda_\tau$; voxel batch size U ; learning rate $\zeta_\theta, \zeta_\eta, \zeta_\tau$; maximal numbers of iterations i_{\max}, k_{\max} ; convergence threshold $\gamma_\beta, \gamma_\theta, \gamma_\eta, \gamma_\tau$; number of stochastic gradient descent (SGD) chains L

Output: estimated main effects $\hat{\beta}(\cdot)$, individual effects $\hat{\alpha}(\cdot)$, noise variances $\hat{\sigma}^2(\cdot)$

Initialize: $\hat{\beta}(\cdot), \hat{\alpha}(\cdot), \hat{\sigma}^2(\cdot) \leftarrow \mathbf{0}$

for $i \leftarrow 1, \dots, i_{\max}$ **do**

$\hat{\beta}_{\text{old}}(\cdot) \leftarrow \hat{\beta}(\cdot)$

$\tilde{\beta}(\mathcal{D}_V) \leftarrow (\mathbf{X}^\top \mathbf{X})^{-1} \{\mathbf{X}^\top [\mathbf{y}(\mathcal{D}_V) - \hat{\alpha}(\mathcal{D}_V)]\}$ // get MUA main effect estimate

for $l \leftarrow 1, \dots, L$ **do**

$\hat{\theta} \sim \mathcal{N}(0, 1)$ // initialize main effect NN parameters

for $k \leftarrow 1, \dots, k_{\max}$ **do**

$\mathbf{d}'_1, \dots, \mathbf{d}'_V \leftarrow \text{shuffle}(\mathbf{d}_1, \dots, \mathbf{d}_V)$; $\mathcal{D}_U \leftarrow \{\mathbf{d}'_1, \dots, \mathbf{d}'_U\}$ // draw voxels

$\Delta \theta \leftarrow \nabla_{\theta} \{\text{tr}[\mathbb{N}(\mathcal{D}_U | \hat{\theta}) - \tilde{\beta}(\mathcal{D}_U)] \mathbf{I} \hat{\sigma}^{-2}(\mathcal{D}_U) [\mathbb{N}(\mathcal{D}_U | \hat{\theta}) - \tilde{\beta}(\mathcal{D}_U)]^\top] + \lambda_\theta \|\hat{\theta}\|_2^2\}$

if $\|\Delta \theta\|_2^2 < \gamma_\theta$ **then** break

$\hat{\theta} \leftarrow \hat{\theta} + \zeta_\theta \Delta \theta$ // update main effect NN parameters with SGD

end

$\hat{\theta}^{(l)} \leftarrow \hat{\theta}$

end

$\hat{\beta}(\cdot) \leftarrow L^{-1} \sum_{l=1}^L \mathbb{N}(\cdot | \hat{\theta}^{(l)})$ // average NNs from multiple SGD chains

if $\|\hat{\beta}(\mathcal{D}_V) - \hat{\beta}_{\text{old}}(\mathcal{D}_V)\|_2^2 < \gamma_\beta$ **then** break

$\tilde{\alpha}(\mathcal{D}_V) \leftarrow \mathbf{y}(\mathcal{D}_V) - \mathbf{X} \hat{\beta}(\mathcal{D}_V)$

$\hat{\eta} \sim \mathcal{N}(0, 1)$ // initialize individual effect NN parameters

for $k \leftarrow 1, \dots, k_{\max}$ **do**

$\mathbf{d}'_1, \dots, \mathbf{d}'_V \leftarrow \text{shuffle}(\mathbf{d}_1, \dots, \mathbf{d}_V)$; $\mathcal{D}_U \leftarrow \{\mathbf{d}'_1, \dots, \mathbf{d}'_U\}$ // draw voxels

$\Delta \eta \leftarrow \nabla_{\eta} \{\text{tr}[\mathbb{N}(\mathcal{D}_U | \hat{\eta}) - \tilde{\alpha}(\mathcal{D}_U)] \mathbf{I} \hat{\sigma}^{-2}(\mathcal{D}_U) [\mathbb{N}(\mathcal{D}_U | \hat{\eta}) - \tilde{\alpha}(\mathcal{D}_U)]^\top] + \lambda_\eta \|\hat{\eta}\|_2^2\}$

if $\|\Delta \eta\|_2^2 < \gamma_\eta$ **then** break

$\hat{\eta} \leftarrow \hat{\eta} + \zeta_\eta \Delta \eta$ // update individual effect NN parameters with SGD

end

$\hat{\alpha}(\cdot) \leftarrow \mathbb{N}(\cdot | \hat{\eta})$

$\mathbf{Z}(\mathcal{D}_V) \leftarrow \mathbf{y}(\mathcal{D}_V) - \mathbf{X} \hat{\beta}(\mathcal{D}_V) - \hat{\alpha}(\mathcal{D}_V)$

$\tilde{\sigma}^2(\mathcal{D}_V) \leftarrow M^{-1} \text{diag}\{\mathbf{Z}(\mathcal{D}_V)^\top \mathbf{Z}(\mathcal{D}_V)\}$ // compute residual variances

$\hat{\tau} \sim \mathcal{N}(0, 1)$ // initialize noise variance NN parameters

for $k \leftarrow 1, \dots, k_{\max}$ **do**

$\mathbf{d}'_1, \dots, \mathbf{d}'_V \leftarrow \text{shuffle}(\mathbf{d}_1, \dots, \mathbf{d}_V)$; $\mathcal{D}_U \leftarrow \{\mathbf{d}'_1, \dots, \mathbf{d}'_U\}$ // draw voxels

$\Delta \tau \leftarrow \nabla_{\tau} \{\|\mathbb{N}(\mathcal{D}_U | \hat{\tau}) - \log[\tilde{\sigma}^2(\mathcal{D}_U)]\|_2^2 + \lambda_\tau \|\hat{\tau}\|_2^2\}$

if $\|\Delta \tau\|_2^2 < \gamma_\tau$ **then** break

$\hat{\tau} \leftarrow \hat{\tau} + \zeta_\tau \Delta \tau$ // update noise variance NN parameters with SGD

end

$\hat{\sigma}^2(\cdot) \leftarrow \mathbb{N}(\cdot | \hat{\tau})$

end

Algorithm 2: NN-ISR model selection procedure

Input: data $\mathbf{X}, \mathbf{y}(\mathcal{D}_V) = \{\mathbf{y}(\mathbf{d}_v)\}_{v=1}^V$, selection relaxedness a , estimated main effects $\hat{\boldsymbol{\beta}}(\cdot)$, individual effects $\hat{\boldsymbol{\alpha}}(\cdot)$, noise variances $\hat{\sigma}^2(\cdot)$

Output: estimated main effects with the unselected voxels set to zero $\bar{\boldsymbol{\beta}}(\mathcal{D}_V)$

$\tilde{\boldsymbol{\beta}}(\mathcal{D}_V) \leftarrow (\mathbf{X}^\top \mathbf{X})^{-1} \{\mathbf{X}^\top [\mathbf{y}(\mathcal{D}_V) - \hat{\boldsymbol{\alpha}}(\mathcal{D}_V)]\}$ // get MUA main effect estimate

$\text{SE}[\tilde{\boldsymbol{\beta}}(\mathcal{D}_V)] \leftarrow \text{diag}[(\mathbf{X}^\top \mathbf{X})^{-1}] \tilde{\sigma}^2(\mathcal{D}_V)$ // MUA main effect standard error

for $q \leftarrow 1, \dots, Q$ **do**

$c_q \leftarrow V^{-1} \sum_{v=1}^V I\{|\tilde{\beta}_q(\mathbf{d}_v)| \geq t_{1-a/2} \text{SE}[\tilde{\beta}_q(\mathbf{d}_v)]\}$ // MUA cutoff quantile

for $v \leftarrow 1, \dots, V$ **do**

$r_q(\mathbf{d}_v) \leftarrow V^{-1} \sum_{w=1}^V I\{|\hat{\beta}_q(\mathbf{d}_v)| \geq |\hat{\beta}_q(\mathbf{d}_w)|\}$ // voxel quantile in NN-ISR

$\bar{\beta}_q(\mathbf{d}_v) \leftarrow \hat{\beta}_q(\mathbf{d}_v) I\{r_q(\mathbf{d}_v) \geq c_q\}$ // select voxel if quantile is high

end

end

$\bar{\boldsymbol{\beta}}(\mathcal{D}_V) \leftarrow [\bar{\boldsymbol{\beta}}_1(\mathcal{D}_V), \dots, \bar{\boldsymbol{\beta}}_Q(\mathcal{D}_V)]^\top$ // concatenate all the covariates

Appendix B Proofs

B.1 Proof for Theorem 1

B.1.1 Preliminaries

We begin with additional notations and definitions for the proof.

Definition 3. Recall the definition of ψ : for independent samples $\{(\mathbf{w}_n, \mathbf{Z}_n)\}_{n=1}^N$ generated from the model $\mathbf{Z}_n = f(\mathbf{w}_n) + \boldsymbol{\epsilon}_n$, where $\boldsymbol{\epsilon}_n$'s are independent and $E(\boldsymbol{\epsilon}_n) = \mathbf{0}$, the empirical optimal weights is

$$\tilde{\boldsymbol{\xi}}_{\mathbf{G},N} = \arg \min_{\boldsymbol{\xi} \in \Xi_{\mathbf{G}}} \left\{ \sum_{n=1}^N \|\aleph(\mathbf{w}_n | \boldsymbol{\xi}_{\mathbf{G}}) - \mathbf{Z}_n\|^2 + \kappa L_{\mathbf{G}}(\boldsymbol{\xi}) \right\}.$$

A total error bound $\psi(\mathbf{G}, N)$ is defined to satisfy

$$\mathbb{E} \left\{ N^{-1} \sum_{n=1}^N \left\| \aleph(\mathbf{w}_n | \tilde{\boldsymbol{\xi}}_{\mathbf{G},N}) - f(\mathbf{w}_n) \right\|^2 \right\} = \mathcal{O}[\psi(\mathbf{G}, N)].$$

Define the theoretical optimal neural network weights to be

$$\boldsymbol{\xi}_{\mathbf{G},N}^* = \arg \min_{\boldsymbol{\xi} \in \Xi_{\mathbf{G}}} \left\{ \sum_{n=1}^N \|\aleph(\mathbf{w}_n | \boldsymbol{\xi}_{\mathbf{G}}) - f(\mathbf{w}_n)\|^2 \right\}.$$

Then we can decompose the total error into approximation and estimation errors: $\psi(\mathbf{G}, N) = \psi^\circ(\mathbf{G}, N) + \psi^*(\mathbf{G}, N)$, where

$$\begin{aligned} \mathbb{E} \left\{ N^{-1} \sum_{n=1}^N \left\| \aleph(\mathbf{w}_n | \boldsymbol{\xi}_{\mathbf{G},N}^*) - f(\mathbf{w}_n) \right\|^2 \right\} &= \mathcal{O}[\psi^\circ(\mathbf{G}, N)]. \\ \mathbb{E} \left\{ N^{-1} \sum_{n=1}^N \left\| \aleph(\mathbf{w}_n | \tilde{\boldsymbol{\xi}}_{\mathbf{G},N}) - \aleph(\mathbf{w}_n | \boldsymbol{\xi}_{\mathbf{G},N}^*) \right\|^2 \right\} &= \mathcal{O}[\psi^*(\mathbf{G}, N)]. \end{aligned}$$

Definition 4. For the NN-ISR model, define

$$\begin{aligned} \boldsymbol{\theta}_{\mathbf{R},V}^* &= \arg \min_{\boldsymbol{\theta} \in \Xi_{\mathbf{R}}} \left\{ \sum_{v=1}^V \|\aleph(\mathbf{d}_v | \boldsymbol{\theta}) - \boldsymbol{\beta}^*(\mathbf{d}_v)\|_2^2 \right\} \\ &= \arg \min_{\boldsymbol{\theta} \in \Xi_{\mathbf{R}}} \left\{ \sum_{v=1}^V [\aleph(\mathbf{d}_v | \boldsymbol{\theta}) - \boldsymbol{\beta}^*(\mathbf{d}_v)]^\top [\aleph(\mathbf{d}_v | \boldsymbol{\theta}) - \boldsymbol{\beta}^*(\mathbf{d}_v)] \right\}. \end{aligned}$$

In addition, let

$$\ell_V^*(\boldsymbol{\theta}) = \frac{1}{V} \sum_{v=1}^V [\aleph(\mathbf{d}_v | \boldsymbol{\theta}) - \aleph(\mathbf{d}_v | \boldsymbol{\theta}_{\mathbf{R},V}^*)]^\top [\aleph(\mathbf{d}_v | \boldsymbol{\theta}) - \aleph(\mathbf{d}_v | \boldsymbol{\theta}_{\mathbf{R},V}^*)].$$

Definition 5. Recall in the NN-ISR model that

$$\begin{aligned}
\hat{\boldsymbol{\theta}}_{\mathbf{R},M,V} &= \underset{\boldsymbol{\theta} \in \Xi_{\mathbf{R}}}{\operatorname{argmin}} \left\{ \sum_{v=1}^V \|\mathbf{X} \aleph(\mathbf{d}_v | \boldsymbol{\theta}) - \mathbf{y}_v\|_2^2 + \lambda L(\boldsymbol{\theta}) \right\} \\
&= \underset{\boldsymbol{\theta} \in \Xi_{\mathbf{R}}}{\operatorname{argmin}} \left\{ \sum_{v=1}^V \|\mathbf{X} \aleph(\mathbf{d}_v | \boldsymbol{\theta}) - \mathbf{X} \boldsymbol{\beta}_v^* - \mathbf{G}_v - \boldsymbol{\epsilon}_v\|_2^2 + \lambda L(\boldsymbol{\theta}) \right\} \\
&= \underset{\boldsymbol{\theta} \in \Xi_{\mathbf{R}}}{\operatorname{argmin}} \left\{ \ell_{M,V}(\boldsymbol{\theta}) + (MV)^{-1} \lambda L(\boldsymbol{\theta}) + \hat{C} \right\},
\end{aligned}$$

where we define

$$\begin{aligned}
\hat{\ell}_{M,V}(\boldsymbol{\theta}) &= \frac{1}{MV} \sum_{v=1}^V [\aleph(\mathbf{d}_v | \boldsymbol{\theta}) - \boldsymbol{\beta}_v^*]^\top \mathbf{X}^\top \mathbf{X} [\aleph(\mathbf{d}_v | \boldsymbol{\theta}) - \boldsymbol{\beta}_v^*] + 2[\aleph(\mathbf{d}_v | \boldsymbol{\theta}) - \boldsymbol{\beta}_v^*]^\top \mathbf{X}^\top (\mathbf{G}_v + \boldsymbol{\epsilon}_v) \\
&= \frac{1}{MV} \sum_{v=1}^V [\aleph(\mathbf{d}_v | \boldsymbol{\theta}) - \aleph(\mathbf{d}_v | \boldsymbol{\theta}_{\mathbf{R},V}^*)]^\top \mathbf{X}^\top \mathbf{X} [\aleph(\mathbf{d}_v | \boldsymbol{\theta}) - \aleph(\mathbf{d}_v | \boldsymbol{\theta}_{\mathbf{R},V}^*)] \\
&\quad + \frac{2}{MV} \sum_{v=1}^V [\aleph(\mathbf{d}_v | \boldsymbol{\theta}) - \aleph(\mathbf{d}_v | \boldsymbol{\theta}_{\mathbf{R},V}^*)]^\top \mathbf{X}^\top \mathbf{X} [\aleph(\mathbf{d}_v | \boldsymbol{\theta}_{\mathbf{R},V}^*) - \boldsymbol{\beta}_v^*] \\
&\quad + \frac{2}{MV} \sum_{v=1}^V [\aleph(\mathbf{d}_v | \boldsymbol{\theta}) - \aleph(\mathbf{d}_v | \boldsymbol{\theta}_{\mathbf{R},V}^*)]^\top \mathbf{X}^\top (\mathbf{G}_v + \boldsymbol{\epsilon}_v)
\end{aligned}$$

and

$$\begin{aligned}
\hat{C} &= \frac{1}{MV} \sum_{v=1}^V [\aleph(\mathbf{d}_v | \boldsymbol{\theta}_{\mathbf{R},V}^*) - \boldsymbol{\beta}_v^*]^\top \mathbf{X}^\top \mathbf{X} [\aleph(\mathbf{d}_v | \boldsymbol{\theta}_{\mathbf{R},V}^*) - \boldsymbol{\beta}_v^*] \\
&\quad + 2[\aleph(\mathbf{d}_v | \boldsymbol{\theta}_{\mathbf{R},V}^*) - \boldsymbol{\beta}_v^*]^\top \mathbf{X}^\top (\mathbf{G}_v + \boldsymbol{\epsilon}_v) + (\mathbf{G}_v + \boldsymbol{\epsilon}_v)^\top (\mathbf{G}_v + \boldsymbol{\epsilon}_v).
\end{aligned}$$

Definition 6. Assume $M = QM'$ for integer M' . Split \mathbf{X} , \mathbf{G}_v , and $\boldsymbol{\epsilon}_v$ evenly into M' batches of size Q , so $\mathbf{X}^T = (\mathbf{X}_1^T, \dots, \mathbf{X}_{M'}^T)$, $\mathbf{G}_v^T = (\mathbf{G}_{v,1}^T, \dots, \mathbf{G}_{v,M'}^T)$, and $\boldsymbol{\epsilon}_v^T = (\boldsymbol{\epsilon}_{v,1}^T, \dots, \boldsymbol{\epsilon}_{v,M'}^T)$. Define

$$\begin{aligned}
\tilde{\boldsymbol{\theta}}_{\mathbf{R},M,V} &= \underset{\boldsymbol{\theta} \in \Xi_{\mathbf{R}}}{\operatorname{argmin}} \left\{ \sum_{v=1}^V \sum_{m=1}^{M'} \|\aleph(\mathbf{d}_v | \boldsymbol{\theta}) - (\mathbf{X}_m^\top \mathbf{X}_m)^{-1} \mathbf{X}_m^\top \mathbf{y}_v\|_2^2 + \lambda L(\boldsymbol{\theta}) \right\} \\
&= \underset{\boldsymbol{\theta} \in \Xi_{\mathbf{R}}}{\operatorname{argmin}} \left\{ \sum_{v=1}^V \sum_{m=1}^{M'} \|\aleph(\mathbf{d}_v | \boldsymbol{\theta}) - \boldsymbol{\beta}^*(\mathbf{d}_v) - (\mathbf{X}_m^\top \mathbf{X}_m)^{-1} \mathbf{X}_m^\top \mathbf{G}_{v,m} - (\mathbf{X}_m^\top \mathbf{X}_m)^{-1} \mathbf{X}_m^\top \boldsymbol{\epsilon}_{v,m}\|_2^2 + \lambda L(\boldsymbol{\theta}) \right\} \\
&= \underset{\boldsymbol{\theta} \in \Xi_{\mathbf{R}}}{\operatorname{argmin}} \left\{ \tilde{\ell}_{M,V}(\boldsymbol{\theta}) + Q(MV)^{-1} \lambda L(\boldsymbol{\theta}) + \tilde{C} \right\}
\end{aligned}$$

where

$$\begin{aligned}\tilde{\ell}_{M,V}(\boldsymbol{\theta}) &= \frac{1}{V} \sum_{v=1}^V [\aleph(\mathbf{d}_v|\boldsymbol{\theta}) - \aleph(\mathbf{d}_v|\boldsymbol{\theta}_{\mathbf{R},V}^*)]^\top [\aleph(\mathbf{d}_v|\boldsymbol{\theta}) - \aleph(\mathbf{d}_v|\boldsymbol{\theta}_{\mathbf{R},V}^*)] \\ &\quad + \frac{2}{V} \sum_{v=1}^V [\aleph(\mathbf{d}_v|\boldsymbol{\theta}) - \aleph(\mathbf{d}_v|\boldsymbol{\theta}_{\mathbf{R},V}^*)]^\top [\aleph(\mathbf{d}_v|\boldsymbol{\theta}_{\mathbf{R},V}^*) - \boldsymbol{\beta}_v^*] \\ &\quad + \frac{2Q}{MV} \sum_{v=1}^V \sum_{m=1}^{M'} [\aleph(\mathbf{d}_v|\boldsymbol{\theta}) - \aleph(\mathbf{d}_v|\boldsymbol{\theta}_{\mathbf{R},V}^*)]^\top (\mathbf{X}_m^\top \mathbf{X}_m)^{-1} \mathbf{X}_m^\top (\mathbf{G}_{v,m} + \boldsymbol{\epsilon}_{v,m})\end{aligned}$$

and \tilde{C} is the sum of the remaining constant terms.

We list below all the sufficient assumptions for the proof of theorems.

Assumption 5. For $m = 1, \dots, M'$,

$$\frac{1}{M^2 V} \sum_{v=1}^V \sum_{m=1}^{M'} \|\mathbf{X}_m^\top \mathbf{G}_{v,m}\|^2 = \mathcal{O}[\psi^*(\mathbf{R}, MV)].$$

Assumption 6. Let each covariate in \mathbf{X}_m be centered and scaled, and let $a_{m,1}, \dots, a_{m,Q}$ be the eigenvalues of $\mathbf{X}_m^\top \mathbf{X}_m$. Then $\bar{a}_m = Q^{-1} \sum_{q=1}^Q a_{m,q} = Q^{-1} \text{tr}(\mathbf{X}_m^\top \mathbf{X}_m) = Q$. There exists a constant $\nu \in (0, 1)$ such that $a_{m,q}/\bar{a}_m \in (1 - \nu, 1 + \nu)$ for all $q = 1, \dots, Q$ and $m = 1, \dots, M'$,

Assumption 7. There exist $v_0, v_1 > 0$ and $\omega \in (0, 1)$ satisfying $0 < v_1 < \omega(1 - \nu)/(1 + \nu)$ such that for V sufficiently large,

$$\left| \tilde{\ell}_{M,V}(\boldsymbol{\theta}) - \ell_V^*(\boldsymbol{\theta}) \right| < v_0 V^{-1} \sum_{v=1}^V \left\| \aleph(\mathbf{d}_v|\tilde{\boldsymbol{\theta}}_{\mathbf{R},M,V}) - \aleph(\mathbf{d}_v|\boldsymbol{\theta}_{\mathbf{R},V}^*) \right\|^2 + v_1 \ell_V^*(\boldsymbol{\theta}).$$

Assumption 8. For MV sufficiently large, $(MV)^{-1} = \mathcal{O}[\psi^*(\mathbf{R}, MV)]$.

We establish the convergence rate of $\aleph(\mathbf{d}_v|\tilde{\boldsymbol{\theta}}_{\mathbf{R},M,V})$ in the lemma below.

Lemma 9. We have

$$\mathbb{E} \left\{ \frac{1}{V} \sum_{v=1}^V \left\| \aleph(\mathbf{d}_v|\tilde{\boldsymbol{\theta}}_{\mathbf{R},M,V}) - \aleph(\mathbf{d}_v|\boldsymbol{\theta}_{\mathbf{R},V}^*) \right\|^2 \right\} = \mathcal{O}[\psi^*(\mathbf{R}, MV)].$$

Proof. Observe that the loss function $\tilde{\ell}_{M,V}$ trains the neural network to fit MV/Q samples that are generated with conditional mean

$$\boldsymbol{\beta}^*(\mathbf{d}_v) + \frac{Q}{M} \sum_{m=1}^{M'} (\mathbf{X}_m^\top \mathbf{X}_m)^{-1} \mathbf{X}_m^\top \mathbf{G}_{v,m}$$

and error $(\mathbf{X}^\top \mathbf{X})^{-1} \mathbf{X}^\top \boldsymbol{\epsilon}_v$ that has mean equal to zero. Thus

$$\mathbb{E} \left\{ \frac{1}{V} \sum_{v=1}^V \left\| \mathbb{N}(\mathbf{d}_v | \tilde{\boldsymbol{\theta}}_{\mathbf{R}, M, V}) - \boldsymbol{\beta}^*(\mathbf{d}_v) - \frac{Q}{M} \sum_{m=1}^{M'} (\mathbf{X}_m^\top \mathbf{X}_m)^{-1} \mathbf{X}_m^\top \mathbf{G}_{v,m} \right\|^2 \right\} = \mathcal{O}[\psi(\mathbf{R}, MV)].$$

Moreover, we have

$$\begin{aligned} \frac{1}{V} \sum_{v=1}^V \left\| \frac{Q}{M} \sum_{m=1}^{M'} (\mathbf{X}_m^\top \mathbf{X}_m)^{-1} \mathbf{X}_m^\top \mathbf{G}_{v,m} \right\|^2 &\leq \frac{Q^2}{M^2 V} \sum_{v=1}^V \sum_{m=1}^{M'} \|(\mathbf{X}_m^\top \mathbf{X}_m)^{-1} \mathbf{X}_m^\top \mathbf{G}_{v,m}\|^2 \\ &\leq \frac{Q^2}{M^2 V} \sum_{v=1}^V \sum_{m=1}^{M'} (1 + \nu) Q^{-1} \|\mathbf{X}_m^\top \mathbf{G}_{v,m}\|^2 \\ &= \mathcal{O}[\psi^*(\mathbf{R}, MV)] < \mathcal{O}[\psi(\mathbf{R}, MV)] \end{aligned}$$

as implied by Assumption 5 and Assumption 6, so

$$\mathbb{E} \left\{ \frac{1}{V} \sum_{v=1}^V \left\| \mathbb{N}(\mathbf{d}_v | \tilde{\boldsymbol{\theta}}_{\mathbf{R}, M, V}) - \boldsymbol{\beta}^*(\mathbf{d}_v) \right\|^2 \right\} = \mathcal{O}[\psi(\mathbf{R}, MV)],$$

which completes the proof by Definition 3. □

B.1.2 Proof

We want to show

$$\mathbb{E} \left\{ \frac{1}{V} \sum_{v=1}^V \left\| \mathbb{N}(\mathbf{d}_v | \hat{\boldsymbol{\theta}}_{\mathbf{R}, M, V}) - \boldsymbol{\beta}^*(\mathbf{d}_v) \right\|^2 \right\} = \mathcal{O}[\psi(\mathbf{R}, MV)].$$

By Assumption 6,

$$\begin{aligned} &\frac{1}{M} [\mathbb{N}(\mathbf{d}_v | \boldsymbol{\theta}) - \mathbb{N}(\mathbf{d}_v | \boldsymbol{\theta}_{\mathbf{R}, V}^*)]^\top \mathbf{X}^\top \mathbf{X} [\mathbb{N}(\mathbf{d}_v | \boldsymbol{\theta}_{\mathbf{R}, V}^*) - \boldsymbol{\beta}_v^*] \\ &= \frac{1}{M} [\mathbb{N}(\mathbf{d}_v | \boldsymbol{\theta}) - \mathbb{N}(\mathbf{d}_v | \boldsymbol{\theta}_{\mathbf{R}, V}^*)]^\top \left(\sum_{m=1}^{M'} \mathbf{X}_m^\top \mathbf{X}_m \right) [\mathbb{N}(\mathbf{d}_v | \boldsymbol{\theta}_{\mathbf{R}, V}^*) - \boldsymbol{\beta}_v^*] \\ &= \frac{1}{M} \sum_{m=1}^{M'} [\mathbb{N}(\mathbf{d}_v | \boldsymbol{\theta}) - \mathbb{N}(\mathbf{d}_v | \boldsymbol{\theta}_{\mathbf{R}, V}^*)]^\top \mathbf{X}_m^\top \mathbf{X}_m [\mathbb{N}(\mathbf{d}_v | \boldsymbol{\theta}_{\mathbf{R}, V}^*) - \boldsymbol{\beta}_v^*] \\ &\in \frac{1}{M} \sum_{m=1}^{M'} (1 \pm \nu) Q [\mathbb{N}(\mathbf{d}_v | \boldsymbol{\theta}) - \mathbb{N}(\mathbf{d}_v | \boldsymbol{\theta}_{\mathbf{R}, V}^*)]^\top [\mathbb{N}(\mathbf{d}_v | \boldsymbol{\theta}_{\mathbf{R}, V}^*) - \boldsymbol{\beta}_v^*] \\ &= (1 \pm \nu) [\mathbb{N}(\mathbf{d}_v | \boldsymbol{\theta}) - \mathbb{N}(\mathbf{d}_v | \boldsymbol{\theta}_{\mathbf{R}, V}^*)]^\top [\mathbb{N}(\mathbf{d}_v | \boldsymbol{\theta}_{\mathbf{R}, V}^*) - \boldsymbol{\beta}_v^*] \end{aligned}$$

Similarly, we have

$$\frac{1}{M} [\mathbb{N}(\mathbf{d}_v | \boldsymbol{\theta}) - \mathbb{N}(\mathbf{d}_v | \boldsymbol{\theta}_{\mathbf{R}, V}^*)]^\top \mathbf{X}^\top \mathbf{X} [\mathbb{N}(\mathbf{d}_v | \boldsymbol{\theta}_{\mathbf{R}, V}^*) - \boldsymbol{\beta}_v^*] \in (1 \pm \nu) [\mathbb{N}(\mathbf{d}_v | \boldsymbol{\theta}) - \mathbb{N}(\mathbf{d}_v | \boldsymbol{\theta}_{\mathbf{R}, V}^*)]^\top [\mathbb{N}(\mathbf{d}_v | \boldsymbol{\theta}_{\mathbf{R}, V}^*) - \boldsymbol{\beta}_v^*]$$

and

$$[\aleph(\mathbf{d}_v|\boldsymbol{\theta}) - \aleph(\mathbf{d}_v|\boldsymbol{\theta}_{\mathbf{R},V}^*)]^\top \mathbf{X}_m^\top (\mathbf{G}_{v,m} + \boldsymbol{\epsilon}_{v,m}) \in (1 \pm \nu) Q \sum_{m=1}^{M'} [\aleph(\mathbf{d}_v|\boldsymbol{\theta}) - \aleph(\mathbf{d}_v|\boldsymbol{\theta}_{\mathbf{R},V}^*)]^\top (\mathbf{X}_m^\top \mathbf{X}_m)^{-1} \mathbf{X}_m^\top (\mathbf{G}_{v,m} + \boldsymbol{\epsilon}_{v,m})$$

Moreover, since

$$\begin{aligned} \left| \tilde{\ell}_{M,V}(\boldsymbol{\theta}) - \ell_V^*(\boldsymbol{\theta}) \right| &= \left| \frac{2}{V} \sum_{v=1}^V [\aleph(\mathbf{d}_v|\boldsymbol{\theta}) - \aleph(\mathbf{d}_v|\boldsymbol{\theta}_{\mathbf{R},V}^*)]^\top [\aleph(\mathbf{d}_v|\boldsymbol{\theta}_{\mathbf{R},V}^*) - \boldsymbol{\beta}_v^*] \right. \\ &\quad \left. + \frac{2Q}{MV} \sum_{v=1}^V \sum_{m=1}^{M'} [\aleph(\mathbf{d}_v|\boldsymbol{\theta}) - \aleph(\mathbf{d}_v|\boldsymbol{\theta}_{\mathbf{R},V}^*)]^\top (\mathbf{X}_m^\top \mathbf{X}_m)^{-1} \mathbf{X}_m^\top (\mathbf{G}_{v,m} + \boldsymbol{\epsilon}_{v,m}) \right| \end{aligned}$$

we have

$$\begin{aligned} &\mathbb{E} \left| \frac{2}{MV} \sum_{v=1}^V [\aleph(\mathbf{d}_v|\boldsymbol{\theta}) - \aleph(\mathbf{d}_v|\boldsymbol{\theta}_{\mathbf{R},V}^*)]^\top \mathbf{X}^\top \mathbf{X} [\aleph(\mathbf{d}_v|\boldsymbol{\theta}_{\mathbf{R},V}^*) - \boldsymbol{\beta}_v^*] \right. \\ &\quad \left. + \frac{2}{MV} \sum_{v=1}^V [\aleph(\mathbf{d}_v|\boldsymbol{\theta}) - \aleph(\mathbf{d}_v|\boldsymbol{\theta}_{\mathbf{R},V}^*)]^\top \mathbf{X}^\top (\mathbf{G}_v + \boldsymbol{\epsilon}_v) \right| \\ &< (1 + \nu) \mathbb{E} \left\{ \left| \tilde{\ell}_{M,V}(\boldsymbol{\theta}) - \ell_V^*(\boldsymbol{\theta}) \right| \right\} \\ &< (1 + \nu) \left\{ v_0 \mathbb{E} \left[V^{-1} \sum_{v=1}^V \|\aleph(\mathbf{d}_v|\tilde{\boldsymbol{\theta}}_{M,V}) - \aleph(\mathbf{d}_v|\boldsymbol{\theta}_{\mathbf{R},V}^*)\|^2 \right] + v_1 \ell_V^*(\boldsymbol{\theta}) \right\} \\ &= (1 + \nu) \{ v_0 \mathcal{O}[\psi^*(\mathbf{R}, MV)] + v_1 \ell_V^*(\boldsymbol{\theta}) \} \\ &< \mathcal{O}[\psi^*(\mathbf{R}, MV)] + \omega(1 - \nu) \ell_V^*(\boldsymbol{\theta}) \end{aligned}$$

by Assumption 7 and Lemma 9. Furthermore,

$$\begin{aligned} &\frac{1}{MV} \sum_{v=1}^V [\aleph(\mathbf{d}_v|\boldsymbol{\theta}) - \aleph(\mathbf{d}_v|\boldsymbol{\theta}_{\mathbf{R},V}^*)]^\top \mathbf{X}^\top \mathbf{X} [\aleph(\mathbf{d}_v|\boldsymbol{\theta}) - \aleph(\mathbf{d}_v|\boldsymbol{\theta}_{\mathbf{R},V}^*)] \\ &\in (1 \pm \nu) \frac{1}{V} \sum_{v=1}^V [\aleph(\mathbf{d}_v|\boldsymbol{\theta}) - \aleph(\mathbf{d}_v|\boldsymbol{\theta}_{\mathbf{R},V}^*)]^\top [\aleph(\mathbf{d}_v|\boldsymbol{\theta}) - \aleph(\mathbf{d}_v|\boldsymbol{\theta}_{\mathbf{R},V}^*)] \\ &= (1 \pm \nu) \ell_V^*(\boldsymbol{\theta}) \end{aligned}$$

so

$$\begin{aligned} \mathbb{E} \left\{ \left| \hat{\ell}_{M,V}(\boldsymbol{\theta}) - \ell_V^*(\boldsymbol{\theta}) \right| \right\} &< \nu \ell_V^*(\boldsymbol{\theta}) + \{ \mathcal{O}[\psi^*(\mathbf{R}, MV)] + \omega(1 - \nu) \ell_V^*(\boldsymbol{\theta}) \} \\ &= [\nu + \omega(1 - \nu)] \ell_V^*(\boldsymbol{\theta}) + \mathcal{O}[\psi^*(\mathbf{R}, MV)] \end{aligned}$$

Since $\ell_V^*(\boldsymbol{\theta})$ has a quadratic form with respect to $\aleph(\mathbf{d}_1|\boldsymbol{\theta}), \dots, \aleph(\mathbf{d}_V|\boldsymbol{\theta})$, we have

$$\begin{aligned} & \mathbb{E} \left\{ \frac{1}{V} \sum_{v=1}^V \left\| \aleph \left(\mathbf{d}_v \left| \arg \min_{\boldsymbol{\theta}} \left\{ \hat{\ell}_{M,V}(\boldsymbol{\theta}) \right\} \right) \right) - \aleph \left(\mathbf{d}_v \left| \arg \min_{\boldsymbol{\theta}} \left\{ \ell_V^*(\boldsymbol{\theta}) \right\} \right) \right\|^2 \right\} \\ &= \frac{2\mathcal{O}[\psi^*(\mathbf{R}, MV)]}{1 - \nu - \omega(1 - \nu)} = \frac{2\mathcal{O}[\psi^*(\mathbf{R}, MV)]}{(1 - \omega)(1 - \nu)} = \mathcal{O}[\psi^*(\mathbf{R}, MV)]. \end{aligned}$$

But $\arg \min_{\boldsymbol{\theta}} \{\ell_V^*(\boldsymbol{\theta})\} = \boldsymbol{\theta}_{\mathbf{R},V}^*$, and as implied by Assumption 8,

$$\mathbb{E} \left\{ \frac{1}{V} \sum_{v=1}^V \left\| \aleph \left(\mathbf{d}_v \left| \arg \min_{\boldsymbol{\theta}} \left\{ \hat{\ell}_{M,V}(\boldsymbol{\theta}) \right\} \right) \right) - \aleph \left(\mathbf{d}_v \left| \hat{\boldsymbol{\theta}}_{\mathbf{R},M,V} \right) \right\|^2 \right\} = \mathcal{O}[\psi^*(\mathbf{R}, MV)].$$

Thus

$$\mathbb{E} \left\{ \frac{1}{V} \sum_{v=1}^V \left\| \aleph \left(\mathbf{d}_v \left| \hat{\boldsymbol{\theta}}_{\mathbf{R},M,V} \right) \right) - \aleph \left(\mathbf{d}_v \left| \boldsymbol{\theta}_{\mathbf{R},V}^* \right) \right\|^2 \right\} = \mathcal{O}[\psi^*(\mathbf{R}, MV)],$$

which gives

$$\mathbb{E} \left\{ \frac{1}{V} \sum_{v=1}^V \left\| \aleph \left(\mathbf{d}_v \left| \hat{\boldsymbol{\theta}}_{\mathbf{R},M,V} \right) \right) - \boldsymbol{\beta}^*(\mathbf{d}_v) \right\|^2 \right\} = \mathcal{O}[\psi(\mathbf{R}, MV)].$$

B.2 Proof for Theorem 2

For any $\mathcal{S} \in \mathcal{D}$, let $\mu(\mathcal{S}) = \int_{\mathbf{d} \in \mathcal{S}} 1 \, d\mathbf{d}$. Without loss of generality, assume $Q = 1$ and $\mu(\mathcal{D}) = 1$. Select $\rho > 0$ to be small enough such that $\mu(\mathcal{A}_\rho) < \delta/4$, where

$$\mathcal{A}_\rho = \{\mathbf{d} \in \mathcal{D} : |\boldsymbol{\beta}^*(\mathbf{d}_v)| \leq 2\rho\}.$$

Moreover, let

$$\begin{aligned} U_v &= \left\| \aleph \left(\mathbf{d}_v \left| \hat{\boldsymbol{\theta}}_{\mathbf{R},M,V} \right) \right) - \boldsymbol{\beta}^*(\mathbf{d}_v) \right\|^2 \\ T_v &= I \left\{ \text{sign} \left[\aleph_\rho \left(\mathbf{d}_v \left| \hat{\boldsymbol{\theta}}_{\mathbf{R},M,V} \right) \right] \right] \neq \text{sign}[\boldsymbol{\beta}^*(\mathbf{d}_v)] \right\}. \end{aligned}$$

Assume that the voxels are evenly located, i.e. for any $\mathcal{S} \in \mathcal{D}$ and $\tau > 0$, there exists a $V_{\mathcal{S},\tau}$ such that for all $V > V_{\mathcal{S},\tau}$,

$$\left| \frac{\frac{1}{V} \sum_{v=1}^V I(\mathbf{d}_v \in \mathcal{S})}{\mu(\mathcal{S})} - 1 \right| \leq \tau.$$

Then by setting $\tau = 1$,

$$\begin{aligned} \frac{1}{V} \sum_{\mathbf{d}_v \in \mathcal{A}_\rho} T_v &\leq \frac{1}{V} \sum_{v=1}^V I(\mathbf{d}_v \in \mathcal{A}_\rho) \\ &\leq (1 + \tau)\mu(\mathcal{A}_\rho) \\ &\leq \delta/2 \end{aligned}$$

for V sufficiently large. Furthermore, we have

$$\begin{aligned}
\mathbb{E} \left[\frac{1}{V} \sum_{\mathbf{d}_v \notin \mathcal{A}_\rho} T_v \right] &= \frac{1}{V} \sum_{\mathbf{d}_v \notin \mathcal{A}_\rho} \Pr [U_v < \rho^2] \\
&\leq \frac{1}{V} \sum_{\mathbf{d}_v \notin \mathcal{A}_\rho} \frac{1}{\rho^2} \mathbb{E}[U_v] \\
&\leq \frac{1}{\rho^2} \frac{1}{V} \sum_{v=1}^V \mathbb{E}[U_v] \\
&= \mathcal{O}[\psi(\mathbf{R}, MV)]
\end{aligned}$$

Hence

$$\begin{aligned}
\Pr \left[\frac{1}{V} \sum_{v=1}^V T_v \geq \delta \right] &= \Pr \left[\frac{1}{V} \sum_{\mathbf{d}_v \notin \mathcal{A}_\rho} T_v \geq \delta - \frac{1}{V} \sum_{\mathbf{d}_v \in \mathcal{A}_\rho} T_v \right] \\
&\leq \Pr \left[\frac{1}{V} \sum_{\mathbf{d}_v \notin \mathcal{A}_\rho} T_v \geq \delta/2 \right] \\
&\leq \frac{2}{\delta} \mathbb{E} \left[\frac{1}{V} \sum_{\mathbf{d}_v \notin \mathcal{A}_\rho} T_v \right] \\
&= \mathcal{O}[\psi(\mathbf{R}, MV)],
\end{aligned}$$

which completes the proof.

B.3 Proof for Theorem 3

This theorem is demonstrated by a modified version of the proof of the convergence theorem for complexity regularization in (Barron, 1991), Pg. 572-573. When applying Craig's variation of Bernstein's inequality in the case of squared error loss, since the input variables x_1, \dots, x_n are fixed in our case, $r(f, f^*)$ needs to be replaced with

$$\mathbb{E}[\bar{U}] = -\mathbb{E}[\hat{r}_n(f, f^*)] = -\mathbb{E} \left[\frac{1}{n} \sum_{i=1}^n [f(x_i) - f^*(x_i)]^2 \right]$$

in Equation (40) and afterwards. At the end, Equation (44) becomes

$$\mathbb{E} \left[\frac{1}{n} \sum_{i=1}^n [f_n(x_i) - f^*(x_i)]^2 \right] \leq \frac{1+\alpha}{1-\alpha} R_n(f^*) + \frac{2\lambda}{n}.$$

With this result, (Barron, 1994; McCaffrey and Gallant, 1994) show that our fixed-design measure of error has the same error bound as in the random-design case, which completes the proof.

Appendix C Experimental setting details

C.1 Simulation studies

C.1.1 Data design

Piecewise continuous (PT) design. The main effect images were divided into 2×2 zones of dimension $16 \times 16 \times 8$, where each zone has one of the following designs: 1) all zeros, 2) a superposition of sharp-edged rectangular regions, 3) a superposition of smooth-edged elliptical regions, and 4) a mixture of 2) and 3). The locations and the values of the non-zero regions were randomly selected. For the individual effects, each individual was randomly assigned with a radiation center from which the voxel values varied linearly. The noises were scaled so that the signal-to-noise ratios of the main effects and the individual effects were 0.05 and 0.25, respectively.

Piecewise constant (PS) design. As originally used in (Zhu et al., 2014), each main effect consisted of constant-valued rectangular regions grouped into 4 square clusters, with the values chosen among 0.0, 0.2, 0.4, 0.6, 0.8, invariant across the third coordinate axis. The individual effects were linear combinations of 3 eigenfunctions and randomly generated coefficients, where each eigenfunction varied only across one of the three coordinate axes.

C.1.2 Experimental settings

Each experimental setup was replicated for 50 times. In each replication, the main effects, individual effects, and noises were where all randomly generated.

Estimation accuracy comparison. We computed the MSE between the true main effects and the estimated main effects by each method. For the PT design, we calculated MSE in each of the 4 zones (empty, smooth, sharp, mixed), averaged across all the 3 main effects. For the PS design, although we computed the MSE in each of the 5 signal levels (0.0, 0.2, 0.4, 0.6, 0.8), we only reported the overall MSE, since it varied little across signal levels.

Selection accuracy comparison. In each main effect, the voxels were ranked by the absolute values of their estimates. (For MUA and SVCN, p-values were used to rank the signal strength of the voxels.) Then the ROC was produced for each main effect based on the ranking. We report the average of all the ROCs across the main effects and across the experimental replicates.

C.1.3 Model tuning

NN-ISR Architecture. Each main and individual effect is independent from each other, i.e. the nodes between them are disconnected. Each hidden layer is activated by LeakyReLU(0.1), followed by a BatchNormalization layer.

NN-ISR Fitting. We used the ADAM optimizer (Kingma and Ba, 2014) in the estimation and selection algorithms. In each stage of training, the optimizer ran up to 2000 epochs and would terminate early if at any point the loss function had decreased by less than 0.001 in the past 100 epochs.

C.2 Real data analysis

After we obtained the estimate by NN-ISR, we ranked the voxels in each main effect by their absolute values. We found the cutoff quantile for each main effect by MUA after setting the FDR to 0.05. Then this cutoff quantile was used to select the voxels for NN-ISR’s estimate. If the quantile was less than 0.05, we selected the strongest signals among

the remaining voxels until 5% of the voxels were selected. For analysis of cognitive ability-associated activation, we also examined each brain function network, which was a union of AAL regions, and calculated the proportion of its voxels that were selected. Inside each network, we also investigated which regions had proportionally the most voxels selected.

C.3 Implementation

The NN-ISR algorithm was implemented in Python by using Keras and other TensorFlow utilities. For SVCM, we used the MATLAB codes provided by the authors of (Zhu et al., 2014). All the experiments were coded in Python. The source code of the NN-ISR software and the experiments in this manuscript will be made publicly available.